JACS
JOURNAL OF THE AMERICAN CHEMICAL SOCIETY
Article
pubs.acs.org/JACS

Solid-State NMR Provides Evidence for Small-Amplitude Slow Domain Motions in a Multispanning Transmembrane α-Helical Protein

Daryl Good,[†,‡] Charlie Pham,[†] Jacob Jagas,[†] Józef R. Lewandowski,[§] and Vladimir Ladizhansky*[,†,‡]

[†]Department of Physics and [‡]Biophysics Interdepartmental Group, University of Guelph, Guelph, Ontario N1G 2W1, Canada
[§]Department of Chemistry, University of Warwick, Coventry CV4 7AL, United Kingdom

Supporting Information

ABSTRACT: Proteins are dynamic entities and populate ensembles of conformations. Transitions between states within a conformational ensemble occur over a broad spectrum of amplitude and time scales, and are often related to biological function. Whereas solid-state NMR (SSNMR) spectroscopy has recently been used to characterize conformational ensembles of proteins in the microcrystalline states, its applications to membrane proteins remain limited. Here we use SSNMR to study conformational dynamics of a seven-helical transmembrane (TM) protein, Anabaena Sensory Rhodopsin (ASR) reconstituted in lipids. We report on site-specific measurements of the ^{15}N longitudinal R_1 and rotating frame $R_{1\rho}$ relaxation rates at two fields of 600 and 800 MHz and at two temperatures of 7 and 30 °C. Quantitative analysis of the R_1 and $R_{1\rho}$ values and of their field and temperature dependencies provides evidence of motions on at least two time scales. We modeled these motions as fast local motions and slower collective motions of TM helices and of structured loops, and used the simple model-free and extended model-free analyses to fit the data and estimate the amplitudes, time scales and activation energies. Faster picosecond (tens to hundreds of picoseconds) local motions occur throughout the protein and are dominant in the middle portions of the TM helices. In contrast, the amplitudes of the slower collective motions occurring on the nanosecond (tens to hundreds of nanoseconds) time scales, are smaller in the central parts of helices, but increase toward their cytoplasmic sides as well as in the interhelical loops. ASR interacts with a soluble transducer protein on its cytoplasmic surface, and its binding affinity is modulated by light. The larger amplitude of motions on the cytoplasmic side of the TM helices correlates with the ability of ASR to undergo large conformational changes in the process of binding/unbinding the transducer.

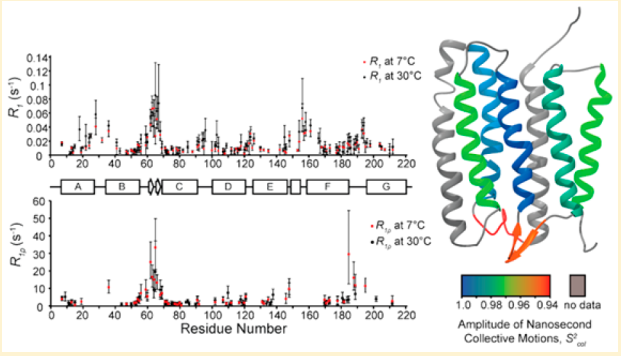

INTRODUCTION

While three-dimensional structures of proteins provide important basic insights into their internal organization, it has been long recognized that internal dynamics play a critical role in protein function. A variety of biological processes such as conformational transitions, allostery, enzymatic activity depend on the proteins' internal plasticity[1−4] on the time scales that span many orders of magnitude.[1,5,6] Because of its functional significance, protein dynamics have attracted considerable attention in recent years. A wide range of experimental methodologies is required in order to capture the dynamic richness of proteins' internal motions.[7−10] In particular, solution nuclear magnetic resonance (NMR) methods have been used extensively to probe dynamics of globular proteins, as described in a number of recently published review articles.[1,3,5,6,11,12]

In systems in which an applicability of solution NMR is limited by slow molecular tumbling, solid-state NMR (SSNMR) is becoming an increasingly popular approach for the characterization of protein dynamics.[13−23] Membrane proteins represent one such class where the study of structure[24−27] and dynamics[23,28−33] remain a challenge. Recent methodological and technological advances in SSNMR, in particular the availability of ultrafast magic angle spinning (MAS) probes capable of achieving spinning rates of 50 kHz and higher,[34,35] and an extensive use of deuteration techniques have paved the way for measuring relaxation rates which are sensitive probes of motions.[13,15,16,36−39] Whereas under moderate spinning frequencies ^{15}N longitudinal and especially transverse relaxation rates, more accurately dubbed coherence lifetimes,[40] are in large part defined by incomplete averaging of coherent interactions, these interactions are effectively suppressed under ultrafast MAS.[35] Specifically, coherent contributions to the $R_{1\rho}$ relaxation rates of ^{15}N[35] and ^{13}C[34] are greatly attenuated at MAS rates greater than 50−60 kHz. Similarly,

Received: April 19, 2017
Published: June 14, 2017

DOI: 10.1021/jacs.7b03974
J. Am. Chem. Soc. 2017, 139, 9246−9258

ultrafast spinning helps suppress rate-averaging effects from proton-driven spin diffusion on the longitudinal R_1 relaxation times measurements (20 kHz for ^{15}N R_1,[41,42] 60 kHz for $^{13}C'$ R_1[43,44]).

Our main focus in this manuscript is on internal dynamics of a lipid-embedded seven transmembrane helical (7TM) receptor Anabaena Sensory Rhodopsin (ASR) from the cyanobacterium *Anabaena* sp. PCC 7120.[45] We have previously used SSNMR order parameter measurements and transverse ^{15}N $R_{1\rho}$ measurements at ultrafast MAS rates of 50 kHz to study internal motions in ASR.[23] We used Simple Model Free and Gaussian Axial Fluctuation[46] analyses to interpret the observed order parameters and elevated $R_{1\rho}$ relaxation rates to estimate time scales of collective motions of the well-defined structural elements such as TM helices and structured loops. TM helices were estimated to move on a time scale on the order of ∼10 ns, whereas two extracellular BC and FG loops were subjected to motions on a time scale of 10−100 ns. The model assumed the collective motions as the dominant relaxation mechanisms, and neglected the contribution from fast local motions to the $R_{1\rho}$ relaxation rates and the dipolar order parameters.

In this report, we expand our measurements to include ^{15}N R_1 measurements at two different fields of 600 and 800 MHz performed at two temperatures of 7 and 30 °C, as well as additional ^{15}N $R_{1\rho}$ data at 30 °C. We interpret the data by modeling ASR dynamics as a combination of fast local (ps) and slower collective (ns) motions. We show that motions in the center and on the extracellular side of helices are dominated by the fast picosecond motions (e.g., they have larger contribution to the overall amplitude), whereas contribution from the nanosecond motions is greater on the cytoplasmic side of helices and in interhelical loop regions.

MATERIALS AND METHODS

Samples. ASR samples were prepared as described previously.[47] Briefly, C-terminally truncated His_6-tagged ASR was expressed in BL21 Codonplus RIL *E. coli* cells grown on M9 minimal medium at 30 °C using 1 g of ^{15}N-labeled ammonium chloride as the sole nitrogen source, and 4 g of either [2-^{13}C]-labeled glycerol, [1,3-^{13}C]-labeled glycerol, or [U−^{13}C]-labeled glucose as carbon sources for alternately (below referred to as 2-ASR and 1,3-ASR, respectively) or uniformly [^{13}C,^{15}N]-labeled ASR samples (UCN ASR), respectively. Protein expression was induced by the addition of IPTG to a final concentration of 1 mM when the cell density reached A_{600} = 0.4 OD. Retinal was added exogenously at a concentration of 7.5 μM at the time of induction. The cells were collected by centrifugation and then treated with lysozyme (0.2 mg/mL) and DNase I (2 μg/mL) before being broken by sonication. The membrane fraction was solubilized in 1% DDM (*n*-dodecyl β-D-maltoside) at 4 °C and purified following the batch procedure described in the Qiagen Ni^{2+}-NTA resin manual. The purified protein was concentrated to approximately 3 mL in a pH 8 buffer containing 5 mM NaCl, 10 mM Tris Base and 0.05% DDM. Liposomes were prepared by hydrating dried DMPC and DMPA mixed in 9:1 ratio (w/w), and mixed with the solubilized ASR at a protein:lipid ratio of 2:1 (w/w) at pH = 8 and stirred at 5 °C for 6 h. The detergent was removed by adding 0.6 mg/mL of Biobeads (SM-II, Bio-Rad Laboratories, Inc., Hercules, CA, USA) and mixing for 24 h. Proteoliposomes were removed from Biobeads by a 27G syringe needle and collected by ultracentrifugation at 150 000*g* for 50 min. The buffer was changed to a pH = 9 (10 mM NaCl and 24 mM CHES), and the sample was further ultracentrifuged into a small pellet at 900 000*g* for 3 h and packed into either thin-walled 3.2 mm or 1.3 mm Bruker rotors.

Site-specific ^{15}N R_1 relaxation measurements were carried out on 1,3-ASR and 2-ASR at two temperatures of 7 and 30 °C. ^{15}N $R_{1\rho}$ relaxation rate measurements were carried out on a UCN ASR at 30 °C. We analyze these results along with previously reported measurements of backbone ^{15}N−^{1}H dipolar order parameters and transverse $R_{1\rho}$ relaxation rates measured at 7 °C,[23] as summarized in Table 1.

Table 1. List of Experiments Used in the Data Analysis

parameter	temperature (°C)	magnetic field strength (MHz)
Dipolar Order Parameter, S^2_{NH} [a]	7	600
^{15}N R_1	7	600
^{15}N R_1	7	800
^{15}N R_1	30	800
^{15}N $R_{1\rho}$ [a]	7	800
^{15}N $R_{1\rho}$	30	800

[a]Previously reported data from ref 23.

NMR Spectroscopy. *Reassignment of Chemical Shifts at 30 °C.* Three-dimensional CANCO and NCACX chemical shift correlation experiments at 30 °C were collected on a Bruker Avance III spectrometer operating at 800 MHz ^{1}H Larmor frequency on a 3.2 mm Efree MAS probe at a spinning rate of 14.3 kHz, using previously published pulse sequences.[48] Sample temperature was calibrated with external references of methanol[49] and KBr,[50] and was maintained at 30 °C.

^{1}H/^{15}N cross-polarization (CP)[51] of 2 ms duration with an ^{15}N field strength of 35 kHz and with the proton field ramped 10% around the n = 2 Hartmann−Hahn (HH)[52] matching condition was used in the NCACX experiment. ^{15}N/$^{13}C_\alpha$ band-selective CP[53] was performed with a 5 ms contact time with a spinlock field on ^{15}N at ∼36 kHz, and with the carbon field intensity ramped linearly (10%) around 22 kHz. DARR (dipolar assisted rotational resonance) recoupling[54,55] of 50 ms was used for ^{13}C−^{13}C mixing.

^{1}H/^{13}C cross-polarization (CP) of 2 ms duration with a ^{13}C field strength of 55 kHz and with the proton field strength ramped linearly (10%) around the n = 2 HH matching condition was used in the CANCO experiment. ^{15}N/$^{13}C_\alpha$ band-selective CP[53] was performed with a 5 ms contact time with a spinlock field on ^{15}N at ∼36 kHz, and with the carbon field ramped linearly (10%) around 22 kHz. The ^{15}N/$^{13}C'$ band-selective CP was performed using the same ^{15}N lock field with the ^{13}C field ramped linearly around 50 kHz, and with the ^{13}C carrier frequency placed at 175 ppm. SPINAL-64 decoupling[56] with a field strength of 84 kHz was used during both the direct and indirect chemical shift evolution periods in all experiments.

Dipolar Order Parameter Measurements at 30 °C. We used TMREV recoupling[57] for ^{1}H−^{15}N order parameter measurements. TMREV recoupling was implemented in a constant time manner with four TMREV elements per rotor cycle (TMREV-4) as shown in Figure S1A, which required proton radio frequency (RF) field strength of ∼96 kHz (90° pulse duration of 2.6 μs). TPPM[58] decoupling of 96 kHz was used during the remainder of the echo period. The total echo period was set to 12 rotor cycles.

TMREV dipolar order parameter measurements require high RF fields, and were carried out using a 3.2 mm MAS TL2 (solenoid) HCN Bruker probe. Because of the sample heating caused by high ^{1}H RF power applied during the dipolar recoupling/decoupling periods, our ASR samples were not sufficiently stable at 30 °C on a time scale of a typical three-dimensional DIPSHIFT experiment (e.g., a series of NCA/NCO 2D planes measured as a function of the dipolar dephasing takes about 6−7 days). We therefore conducted two-dimensional TMREV experiments (e.g., a series of 1D spectra as a function of TMREV dipolar dephasing takes about 1 h) to probe overall dynamics in the protein. These measurements were performed at 30 °C and repeated at 7 °C on a Bruker Avance III 600 MHz spectrometer, at a spinning rate of 8 kHz.

Longitudinal ^{15}N Relaxation Measurements at 7 and 30 °C. ^{15}N R_1 relaxation rate measurements were carried out using Bruker 3.2 mm

DOI: 10.1021/jacs.7b03974
J. Am. Chem. Soc. 2017, 139, 9246−9258

MAS Efree triple resonance probes at two fields corresponding to ^{1}H Larmor frequencies of 600 and 800 MHz, and at two temperatures of 7 and 30 °C. For each of the fields and temperatures, a series of 2D NCA and NCO afterglow[59] correlation spectra were recorded as a function of recovery delays of 1, 5, 10, 20, and 30 s using a pulse sequence shown in Figure S1B. Samples were spun at a MAS rate of 19 kHz to minimize the rate-averaging effects from ^{15}N−^{15}N proton driven spin diffusion.[41,42]

^{15}N $R_{1\rho}$ Relaxation Measurements at 30 °C. ^{15}N $R_{1\rho}$ relaxation rate measurements at 30 °C were performed at 800 MHz ^{1}H Larmor frequency using a Bruker 1.3 mm MAS triple resonance probe, with ^{15}N spin lock of 12 kHz, and at a spinning rate of 55 kHz. A series of 2D NCACB correlation spectra were recorded as a function of spinlock times of 0.02, 50, 100, 200, and 300 ms using a pulse sequence shown in Figure S1C. TPPM48 decoupling[60] at a power set to approximately a quarter of the spinning frequency was used in the direct and indirect chemical shift evolution dimensions. DREAM mixing[61,62] was used to induce $^{13}C_{\alpha}/^{13}C_{\beta}$ transfer by applying a 3.5 ms (pulse length was optimized experimentally) pulse of a tangential shape centered at 27.5 kHz, with ^{13}C carrier frequency set at 45 ppm.

Data Analysis. All 2D and 3D chemical shift correlation spectra were processed with NMRPipe[63] using Lorentzian-to-Gaussian apodization functions. Peak amplitudes were extracted using the CARA software.[64] Overlapping peaks were fit to multiple Gaussian functions and linear deconvolution was performed to estimate the amplitude of each peak.

In all relaxation experiments, peak amplitudes were fit to a single exponential decay function, where the fit parameters were the relaxation rate and an overall amplitude scaling factor.

Peak amplitudes extracted from TMREV experiments were fit to the theoretical three-spin model of the TMREV dipolar recoupling which takes into account couplings to the directly bonded and one remote protons.[57,65] The fit parameters were the dipolar coupling constant to the directly bonded proton, effective relaxation constant and an overall amplitude scaling factor. The dipolar order parameters were determined by comparing the best fit dipolar coupling constant with the known dipolar coupling constant in the static limit using 1.02 Å N−H bond length.[66]

The effects of random noise on the best fit R_1, $R_{1\rho}$, and order parameters results were assessed with Monte Carlo simulations using an in-house written program. Gaussian-distributed random noise with a width determined by the experimental root-mean-square noise was added to the best fit theoretical signal to produce an array of 5000 simulated signals. The simulated signals were refit to theoretical models to determine the distribution of the fit parameters that result from random spectral noise. Errors are reported at the 95% confidence level.

RESULTS

Spectroscopic Assignments and Structural Perturbations at 30 °C. We have previously shown that ASR forms stable trimers,[67−69] which arrange into 2D crystalline domains with a characteristic domain size of ∼50 nm.[69] ASR remains in a trimeric state at 30 °C (as evident for example, from the characteristic bilobe CD spectra in the visible range[67]), and this prevents the protein from rapid axial diffusion in the bilayer. Accordingly, the analysis of the ^{15}N sideband patterns indicate full strengths of the CSA tensors for these nuclei (Figure S2).

We have previously reported spectroscopic assignments of ASR at 5 °C (the amino acid sequence, secondary structure and assignments are summarized in Figure S3),[47,70] and they remain unchanged at 7 °C. We observed, however, that at a higher temperature of 30 °C the intensities of cross peaks decrease, and many cross peaks show small but noticeable shifts. To confidently reassign peaks and track any possible structural changes, we have carried out three-dimensional CANCO and NCACX experiments at 30 °C, and were able to reassign the majority of peaks using chemical shift mapping. Temperature dependent chemical shift perturbations occur throughout the protein but remain within 0.9 and 1.5 ppm for carbon atoms (C_{α}, C_{β}, C′) and ^{15}N, respectively (Figure S4). Overall, the changes in chemical shifts do not correspond to any large changes in secondary structure, with the extents of helices and local structural deviations from helicity remaining essentially at the same positions. Specifically, the structure of the BC loop remains β-hairpin, and the FG loop shows some β-secondary structure albeit not as well-defined as in the BC loop.

The elevated temperature has much more pronounced effect on signal intensities than it does on chemical shifts. The efficiency of ^{1}H/^{15}N and ^{1}H/^{13}C CP excitation decreases by about 10−15%, whereas the efficiency of ^{15}N/^{13}C CP decreases by ∼20%, overall resulting in about 40% attenuation of the signal in the CANCO experiment (see Figure S4A). This signal attenuation occurs because of the overall significant reduction of coherence lifetimes for ^{1}H, ^{15}N, and ^{13}C as evident from the bulk $R_{1\rho}$ measurements at a spinning rate of 14.3 kHz. $R_{1\rho}$ relaxation rates of ^{1}H, ^{15}N, and ^{13}C increase, respectively, from 133, 27, and 36 s^{-1} at 7 °C to 157, 39 to 60 s^{-1} at 30 °C (see Figure S5).

Conformational Dynamics of ASR at 7 °C. Our previous measurements of conformational dynamics of ASR at 7 °C included dipolar order parameters for ^{1}H−^{15}N, ^{13}C−^{1}H, ^{15}N−^{13}C′ and ^{15}N−$^{13}C\alpha$ bonds to probe amplitudes of submicrosecond motions, as well as ^{15}N $R_{1\rho}$ measurements at a spinning rate of 50 kHz to probe the time scale of slower conformational motions on the nanosecond-microsecond time scale.[23] The site-specific S^2_{CH} and S^2_{NH} order parameters varied between 0.7 and 0.9 along the protein sequence, and were generally consistent with the rigid backbone (e.g., subjected to submicrosecond motions of small amplitudes) for both TM and loop regions. The ^{15}N $R_{1\rho}$ relaxation rates values indicated the presence of slower motions for the extracellular BC and FG loops, and suggested that slow motions can also contribute to the $R_{1\rho}$ relaxation of the TM backbone. However, the limited scope of experimental data precluded us from accurately quantifying the extent of slow motions, whereas the effect of fast motions was completely neglected. Here, we conducted additional measurements of ^{15}N R_1 relaxation rates which report on the motions occurring on the fast picosecond to nanosecond time scale, and combine the order parameters, R_1 and $R_{1\rho}$ rates to model the motions.

The general trends in relaxation discussed below can be qualitatively rationalized in a framework of the Simple Model Free (SMF) model. We use the theoretical description for R_1 and $R_{1\rho}$ derived by Kurbanov et al.,[71] in which an ^{15}N spin relaxes due to its chemical shift anisotropy, and due to the through-space couping to a single proton ^{1}H under magic angle spinning conditions. These expressions for $R_{1\rho}$ are generally accurate for most time scales except when the correlation time approaches the time scale defined by the inverse of the rotor fequency. In the latter case, the theoretical expression below result in somewhat overestimated $R_{1\rho}$ values compared to the exact numerical simulations.[13] These deviations are negligible for the time scales estimated for ASR.[13,19] We therefore use the expressions below without any corrections:

$$R_1 = \frac{1}{T_1} = R_1^{CSA} + R_1^{NH} \quad (1)$$

DOI: 10.1021/jacs.7b03974
J. Am. Chem. Soc. 2017, 139, 9246−9258

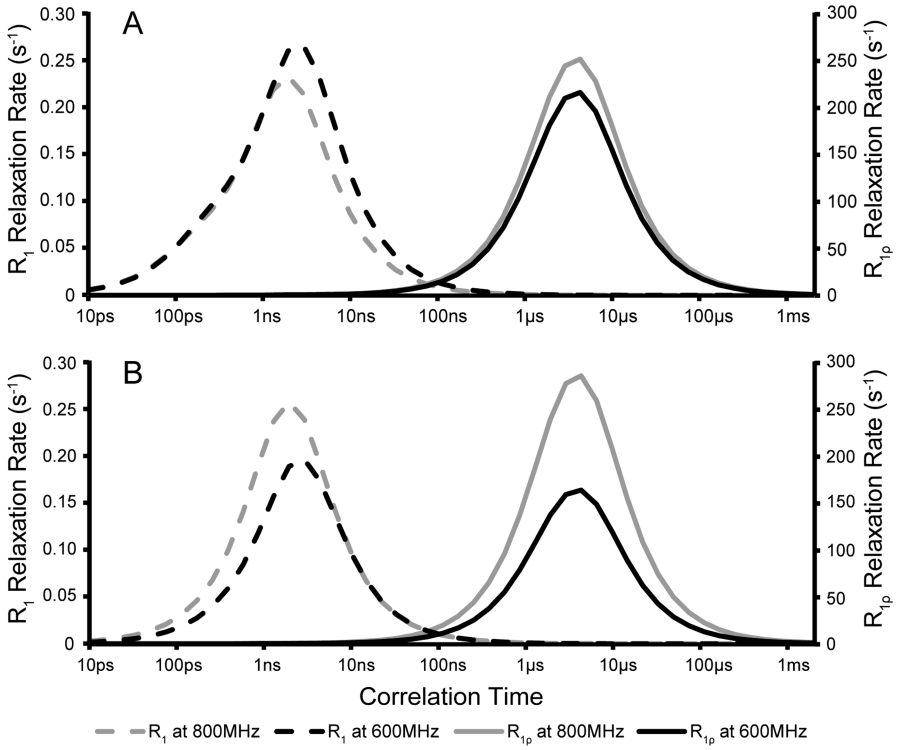

Figure 1. ^{15}N R_1 and $R_{1\rho}$ theoretical curves calculated using Simple Model Free approach (eqs 1−7) as a function of correlation time at two fields corresponding to ^{1}H Larmor frequencies of 800 and 600 MHz for a typical S^2_{NH} order parameter of 0.9. (A) R_1 and $R_{1\rho}$ are calculated for ^{15}N−^{1}H moieties and taking into account ^{15}N chemical shift anisotropy. In this case, dipolar interaction is the dominant relaxation mechanism. (B) R_1 and $R_{1\rho}$ are calculated for deprotonated moieties (e.g., prolines) taking into account only ^{15}N chemical shift anisotropy, using eq 7 for the spectral density function, and assuming the same order parameter S^2_{CSA} of 0.9. Note that the field dependent region of the R_1 is shifted toward the faster time scales.

$$R_{1\rho} = \frac{1}{T_{1\rho}} = \frac{1}{2}R_1 + R_{1\rho}^{CSA} + R_{1\rho}^{NH} \tag{2}$$

Here R_1^{CSA} and R_1^{NH} are contributions to the longitudinal relaxation rates resulting from the anisotropic chemical shift and dipolar coupling, and $R_{1\rho}^{CSA}$ and $R_{1\rho}^{NH}$ are the CSA and dipolar contributions to the $R_{1\rho}$ relaxation. We approximate the CSA tensor as axially symmetric, and these contributions can be written as

$$R_1^{CSA} = \frac{3}{4}(\delta_{CSA}\omega_N)^2 J(\omega_N) \tag{3}$$

$$R_1^{NH} = \frac{\delta_{NH}^2}{4}(J(\omega_H - \omega_N) + 3J(\omega_N) + 6J(\omega_H + \omega_N)) \tag{4}$$

$$R_{1\rho}^{CSA} = \frac{(\delta_{CSA}\omega_N)^2}{4}\left(\frac{1}{3}J(\omega_1 - 2\omega_r) + \frac{2}{3}J(\omega_1 - \omega_r) + \frac{2}{3}J(\omega_1 + \omega_r) + \frac{1}{3}J(\omega_1 + 2\omega_r)\right) \tag{5}$$

$$R_{1\rho}^{NH} = \frac{\delta_{NH}^2}{4}\left(3J(\omega_H) + \frac{1}{3}J(\omega_1 - 2\omega_r) + \frac{2}{3}J(\omega_1 - \omega_r) + \frac{2}{3}J(\omega_1 + \omega_r) + \frac{1}{3}J(\omega_1 + 2\omega_r)\right) \tag{6}$$

Here, ω_1 is the spinlock field amplitude expressed in rad/s (small off-resonance effects are neglected), $\omega_r/2\pi$ is the spinning frequency, and ω_H and ω_N are the Larmor frequencies of ^{1}H and ^{15}N, respectively; δ_{CSA} is the reduced chemical shift anisotropy (−109 ppm) for backbone amide ^{15}N,[72] and δ_{NH} is the dipolar coupling constant of 11.478 kHz for the ^{15}N−^{1}H spin pair corresponding to the N−H bond length of 1.02 Å. Systematic errors related to small site-specific variation in ^{15}N chemical shift anisotropy were found to result in small $R_1/R_{1\rho}$ variations,[73] which are well within the confidence intervals.

In the SMF approach, the motions are modeled as isotropic using a single time scale and order parameter. Assuming exponential autocorrelation function, the spectral density can be written as[74,75]

$$J(\omega) = \frac{2}{5}(1 - S^2_{NH})\frac{\tau_{c,eff}}{1 + \omega^2\tau^2_{c,eff}} \tag{7}$$

where S^2_{NH} is the order parameter that was determined experimentally using DIPSHIFT spectroscopy,[23] and $\tau_{c,eff}$ is the effective correlation time. R_1 and $R_{1\rho}$ relaxation rates calculated according to eq 1−7 as a function of motional correlation time and field strength for a typical S^2_{NH} of 0.9 are shown in Figure 1A. Similar expression (with the dipolar order parameter replaced by the CSA order parameter) was used to calculate curves in Figure 1B for deprotonated moieties.

First, we anticipate that significant nanosecond motions will result in the field-dependent dipolar-driven longitudinal relaxation for nonproline residues, with faster relaxation at a lower field. No such dependence is expected to result from fast picosecond motions (Figure 1A). Second, we anticipate different trend for prolines, whose ^{15}N amide relaxation is primarily governed by the CSA effects. In this case, strong field dependence is anticipated from motions on a time scale shorter than ∼10 ns, whereas motions in the slower regime (>10 ns) would be field-independent (Figure 1B).

DOI: 10.1021/jacs.7b03974
J. Am. Chem. Soc. 2017, 139, 9246−9258

It was pointed out before that proton driven spin diffusion can lead to averaging of the ^{15}N longitudinal nuclear relaxation rates at slow to moderate spinning rates. To minimize these effects, the ^{15}N R_1 measurements were carried out at a spinning rate of 19 kHz.[42] R_1's were measured at two field strengths of 600 and 800 MHz in two samples of 1,3-ASR and 2-ASR. 101 and 108 cross peaks could be cumulatively resolved in the 2D spectra at 600 and 800 MHz field strengths, respectively. Typical relaxation trajectories are shown in Figure 2A–C.

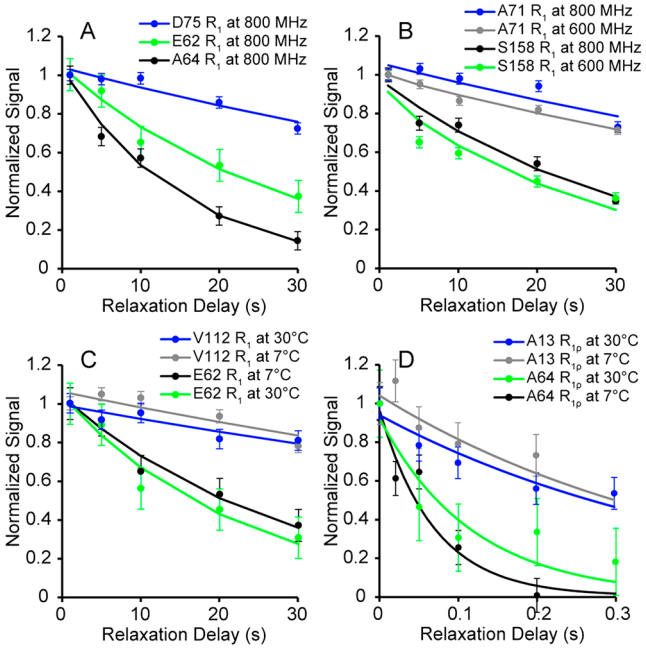

Figure 2. ^{15}N R_1 and $R_{1\rho}$ relaxation measurements and the corresponding best fits at 600 and 800 MHz and at two temperatures of 7 and 30 °C. Solid circles represent experimental point whereas solid lines are best fit simulations. (A) R_1 relaxation trajectories for D75 in helix C, and for E62 and A64 of the BC loop. (B) R_1 trajectories for S158 in the EF loop and A71 in helix C as a function of the magnetic field. (C) R_1 relaxation trajectories for residues V112 in helix C and E62 in the BC loop measured at two temperatures. (D) $R_{1\rho}$ relaxation trajectories for residues A13 in helix A and A64 in the BC loop measured at two temperatures.

In Figure 3A,B we show site-specific ^{15}N R_1 values of ASR measured at two different fields corresponding to ^{1}H Larmor frequencies of 600 and 800 MHz, and $R_{1\rho}$ values which were measured at 800 MHz. These values are also summarized in Table S2. The extracted R_1 values share common features at both fields. First, they vary significantly between the transmembrane and exposed regions. Typical average values calculated for each of the seven helices are in the range of 0.010–0.015 s^{-1} indicating a rigid TM protein backbone with limited motions. These values are considerably smaller than those reported for the rigid backbone of microcrystalline GB1 under similar conditions,[34] suggesting that motions in the TM domain of ASR are more restricted, which could be due to the different environment of helices in tightly coupled ASR trimers, which are packed into a hexagonal lattice.[68]

Second, the R_1 values in the central portions of TM helices are similar at 600 MHz and at 800 MHz, indicating that the rates are dominated by fast motions in the picosecond range. In this case picosecond motions account for the majority of the measured dipolar order parameters, and any nanosecond motions if present, are likely characterized by small amplitudes. In contrast, the R_1 values in the loop regions show some field dependence, and are generally higher at the lower 600 MHz field strength, suggesting, according to the SMF predictions (Figure 1A), that slower nanosecond motions contribute significantly to the longitudinal relaxation in loops.

Third, R_1 rates are consistently higher toward the water exposed ends of helices and in the loop regions, varying at 600 MHz from 0.019 s^{-1} for the cytoplasmic CD loop (residues 91–100), to 0.030 s^{-1} for the short extracellular DE loop (residues 121–124), to 0.039 s^{-1} for the extracellular beta-hairpin in the BC loop (residues 56–70) (Table S3). This enhancement of relaxation rates shows good correlation with the hydrogen/deuterium (H/D) exchange data which were presented by us previously,[47,68] and are shown in Figure 3C. The reduction of cross peak intensities in the H/D exchange experiments occurs because amide protons are replaced with deuterons, and is primarily observed for the loop regions and exposed flanks of helices. This enhanced exchangeability is associated with solvent accessibility (e.g., exposure of the loops or transient local structural opening of the protein core), and in addition requires the breakage of hydrogen bonds.[2,8] The latter event is likely to be correlated with enhanced local mobility of the NH bonds.

This expected increase in fast local mobility is accompanied by the increase of nanosecond motions amplitude, as evident from the elevated ^{15}N $R_{1\rho}$ relaxation rates (representative relaxation trajectories are shown in Figure 2D) which are sensitive to slower motions on the nanosecond to microsecond time scale (data available only for the BC and FG loops and for residues in the flanks of helices A and F, see Figure 3B), as well as from the apparent dependence of the R_1 rates on the magnetic field, with generally greater rates at a lower field as expected for residues with contributions from slower motions (Figure 3A, Table S2).

Interestingly, a different trend in the R_1 field dependence is observed for prolines (Figure 3A, inset) whose ^{15}N relaxation is dominated by the ^{15}N CSA. Elevated R_1's with pronounced field dependence (greater values at the higher field of 800 MHz) are observed for P29, P33, P149 in the loop regions indicating the presence of fast motions (τ_c < 10 ns). Similar trend was previously observed for the R_1 relaxation rates of the carbonyl atoms in GB1.[34] R_1 of P187 in the FG loop is high and field-independent, suggesting that the slow motion is much more pronounced for this loop. Finally, R_1 rates of the TM prolines P44, P81 and P180 are very small, which is consistent with motions of small amplitudes, whereas the field dependence cannot be stated because of the large experimental uncertainty.

In summary, qualitative analysis of R_1 and $R_{1\rho}$ relaxation rates provides evidence of both slow nanosecond and fast picosecond time scale motions: elevated R_1 values and the field dependence of the proline R_1's in the loop regions suggest the presence of fast picosecond motions, whereas elevated $R_{1\rho}$ rates and the field dependence of R_1 relaxation rates of nonproline residues in the loops suggest contributions of slower nanosecond motions. In contrast, lower relaxation R_1 and $R_{1\rho}$ rates and lack of field dependence for both proline and nonproline residues in the TM helices indicate that the amplitudes of slow nanosecond motions are small in TM regions.

Dynamics at 30 °C. To gain further insights into ASR dynamics and solidify our preliminary conclusions regarding the presence of the nanosecond motions, we now proceed to the discussion of temperature dependence of relaxation rates. In

DOI: 10.1021/jacs.7b03974
J. Am. Chem. Soc. 2017, 139, 9246–9258

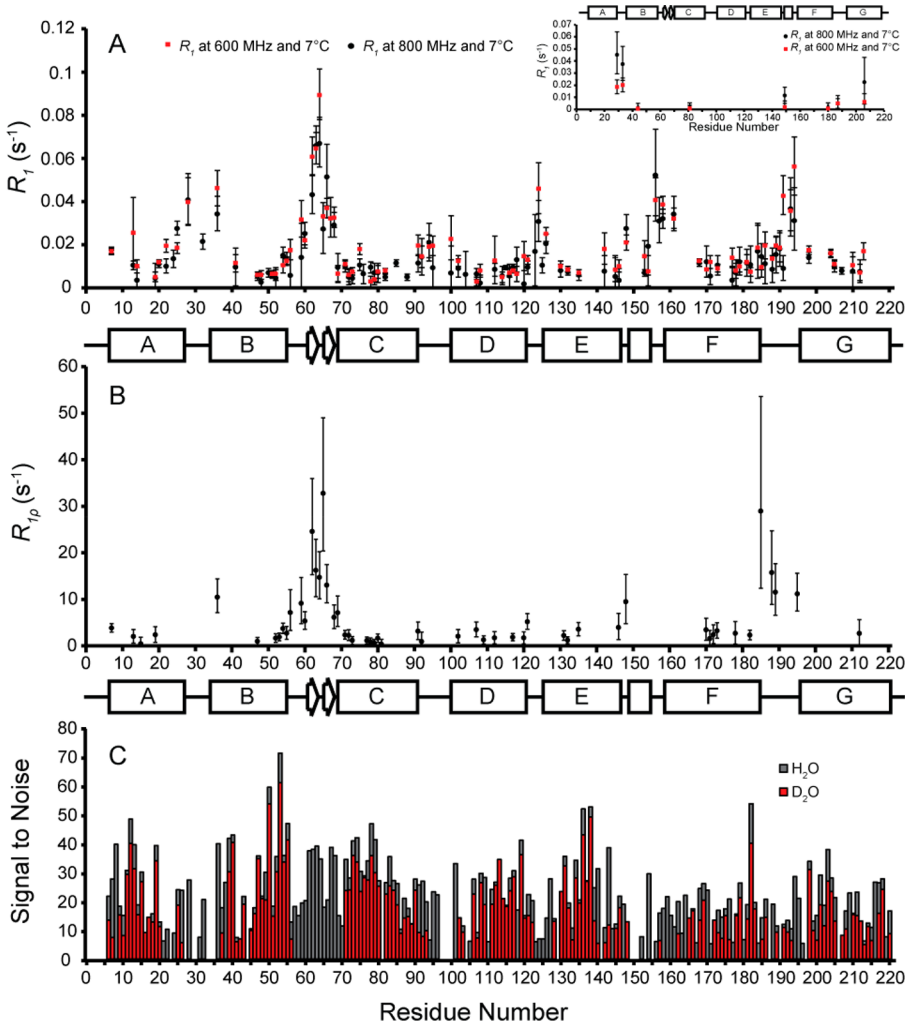

Figure 3. (A) Site-specific R_1 relaxation rates on 600 and 800 MHz spectrometers at 7 °C. R_1 rates of nonprolyl residues are shown on the main graph, whereas R_1's of prolines are shown separately as an inset. (B) Site-specific $R_{1\rho}$ relaxation rates determined at 7 °C, using ^{15}N lock field of 12 kHz at a spinning rate of 50 kHz. Reprinted with permission from D. Good, et al. *J. Am. Chem. Soc.* **2014**, *136*, 2833. Copyright 2014, American Chemical Society. (C) A comparison of cross peak intensities in the 2D NCA and 3D NCACX experiments on ASR incubated in H_2O (gray) and D_2O (red) buffers. NCA and NCACX experiments were recorded with short HN CP excitation of 300 μs to ensure that the cross peaks primarily originate from amide protons. Additional details can be found in refs 47, 68.

Figure 2C,D we show representative R_1 and $R_{1\rho}$ relaxation trajectories at 7 and 30 °C, and in Figures 4, S9 we compare site-specific R_1 and $R_{1\rho}$ rates at the two temperatures. Representative NMR spectra are shown in Figure S8.

At higher temperatures relaxation rates can be affected by both changes in the order parameters, as well as by the changes in the time scale of motions. We first investigated the change in the order parameters using TMREV dipolar recoupling. Because of the power limitations of the 3.2 mm Bruker Efree probe, TMREV measurements had to be carried out on a TL2 solenoid probe. Our attempts to record site-specific TMREV data at 30 °C using NCA/NCO spectroscopies were unsuccessful due to significantly reduced lifetime of samples at the elevated temperature and under high power RF irradiation (measurements on two ASR samples were attempted, and both resulted in sample degradation).

To evaluate the general trend of the order parameter changes as a function of temperature, we used 1D ^{15}N detected and $^{13}C\alpha$-detected (e.g., TMREV dephasing followed by an $^{15}N/^{13}C\alpha$ polarization transfer) $^{15}N-^{1}H$ dipolar recoupling TMREV measurements at 7 °C and at 30 °C. We observed similar TMREV dephasing for the bulk signals at 7 and 30 °C (Figure S7, Table S1), which suggests only small changes in motional amplitudes. Additional discussion is given in the Supporting Information.

Although similar bulk TMREV behavior at 7 and 30 °C cannot serve as hard evidence that the site-specific amplitudes of motions do not change as a function of temperature, it does suggest that the main effect of temperature on the motions is through changes in the time scale of motions as expected from the Arrhenius relation:

$$\tau_c(303\ \mathrm{K}) = \tau_c(280\ \mathrm{K})\cdot\exp\left(\frac{E_a}{R}\left(\frac{1}{303} - \frac{1}{280}\right)\right) = \tau_c(280\ \mathrm{K})\cdot\exp\left(\frac{-0.00027E_a}{R}\right) \quad (8)$$

Here, $\tau_c(303\ \mathrm{K})$ and $\tau_c(280\ \mathrm{K})$ are the correlation times at 30 °C (303 K) and 7 °C (280 K), respectively, E_a is the activation energy, and R is the universal gas constant. According to eq 8, we thus expect that correlation times would become shorter at higher temperatures. Whereas the reduction of both the

DOI: 10.1021/jacs.7b03974
J. Am. Chem. Soc. 2017, 139, 9246−9258

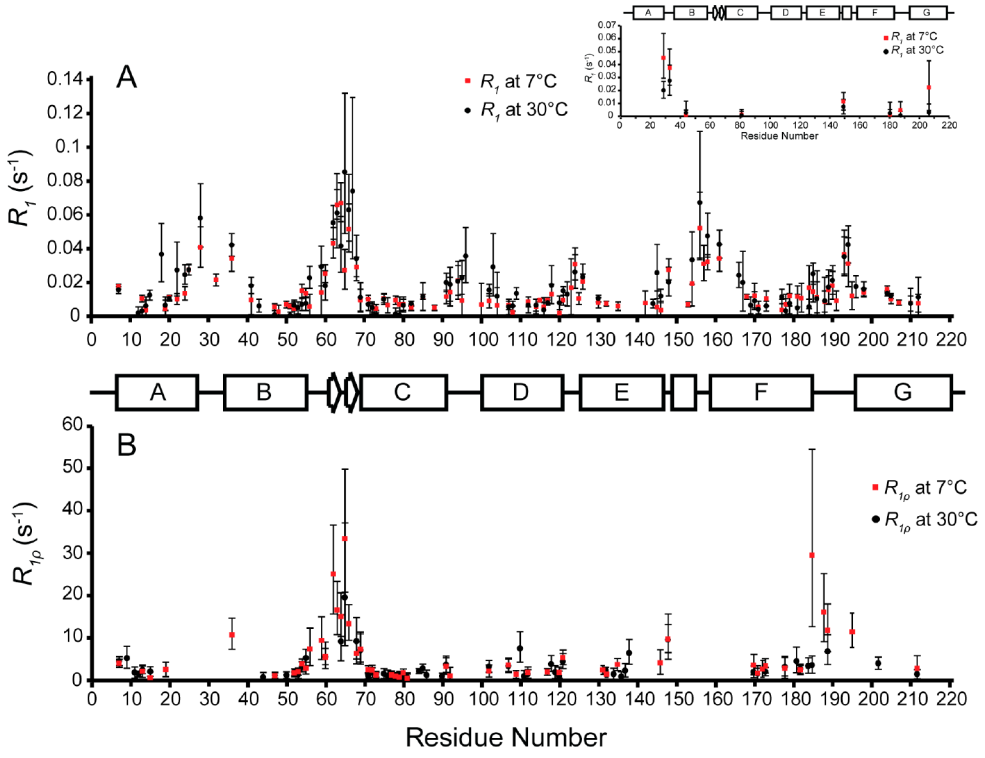

Figure 4. Backbone ^{15}N R_1 (A) and $R_{1\rho}$ (B) relaxation rates measured on a 800 MHz spectrometer, and at 7 °C (red squares) and 30 °C (black circles). R_1 relaxation rates for prolines are shown in the inset of panel A.

nanosecond and picosecond correlation times would result in a decrease of $R_{1\rho}$ rates (Figure 1), the behavior of R_1 is expected to be dependent on the motional regime: if picosecond time scale motion dominates the R_1 relaxation pathway, a shorter correlation time would result in a decrease of R_1. To the contrary, for residues with relaxation dominated by slower nanosecond motions with correlation times beyond the T_1 minimum (e.g., correlation times on the order of 10 ns or longer in Figure 1A), shortening of the correlation time would cause an increase of R_1.

We observe a small decrease of R_1 rates at higher temperature in the middle portions of TM helices (e.g., for helices C, D and F) (Figures 4, S9). In contrast, R_1 rates increase significantly with temperature in the cytoplasmic ends of helices A, B, C, D and F, and in most interhelical loops, suggesting an increased contribution from slower motions. This is further supported by the observed decrease of $R_{1\rho}$ rates, especially pronounced for the BC and FG loops (Figures 4, S9). The short CD loop (see Table S4), is the only exception from this trend, and this may be due to it being more sterically constrained.

There are a small number of residues in both the TM helical regions and in the interhelical loop regions which do not follow these general trends. The most likely reasons for this to occur are related to either a large uncertainty in the experimental data or the presence of additional slower (e.g., microsecond) time scale motions, which are not present at 7 °C, but get activated at the higher temperature. For example, such activation processes may be related to changes in the state of lipids, since the DMPC lipid phase transition temperature is 24 °C.

Modeling of Relaxation Rates Using Simple Model Free Approach. For SMF analysis we only consider residues for which at least five out of the six measurements summarized in Table 1 are available (41 residues only, primarily due to the signal-to-noise limitations of the ^{13}C-detection in a small 1.3 mm rotor[76]). We assume that the order parameters S^2_{eff} remain the same at 7 and 30 °C, and that the correlation times at 7 and 30 °C are related through the Arrhenius relation of eq 8. By minimizing the χ^2 (eq S1, Supporting Information) we simultaneously fit the order parameter S^2_{eff}, correlation time $\tau_{c,\text{eff}}$ and activation energy E_a for each residue.

In evaluating whether the SMF model can satisfactorily explain the observed data, we used the following two criteria: first, back-calculated best fit values should agree with the experimentally measured values (i.e., the reduced χ^2 value corresponding to the root mean squared difference between back-calculated and experimental values should be close to or less than 1); second, the predicted time scale should be consistent within a given secondary structure element (i.e., TM helices or BC and FG loops), as inconsistent results among neighboring residues that experience a similar physical environment are likely an indication of multiple motional time scales which cannot be accounted for accurately by the SMF.

In Figures 5A–C, S11 we show experimental and back-calculated relaxation rates and order parameters, whereas the dominant time scales extracted from Monte Carlo simulations are shown in Figure 5D. Details of the Monte Carlo fitting procedure is given in the Supporting Information with typical representative histograms of the Monte Carlo fits shown in Figure S10. Overall, the back calculated relaxation rates and the order parameters do not precisely reproduce the observed experimental data for residues located in the transmembrane regions of the protein with reduced χ^2 values (Table S6, Figure S12) for most residues being greater than 5. The large values of the reduced χ^2 reflect the fact that the experimental data are not well described by the SMF with a single motion, and that the backbone amides undergo motions on two or more time scales;

DOI: 10.1021/jacs.7b03974
J. Am. Chem. Soc. 2017, 139, 9246–9258

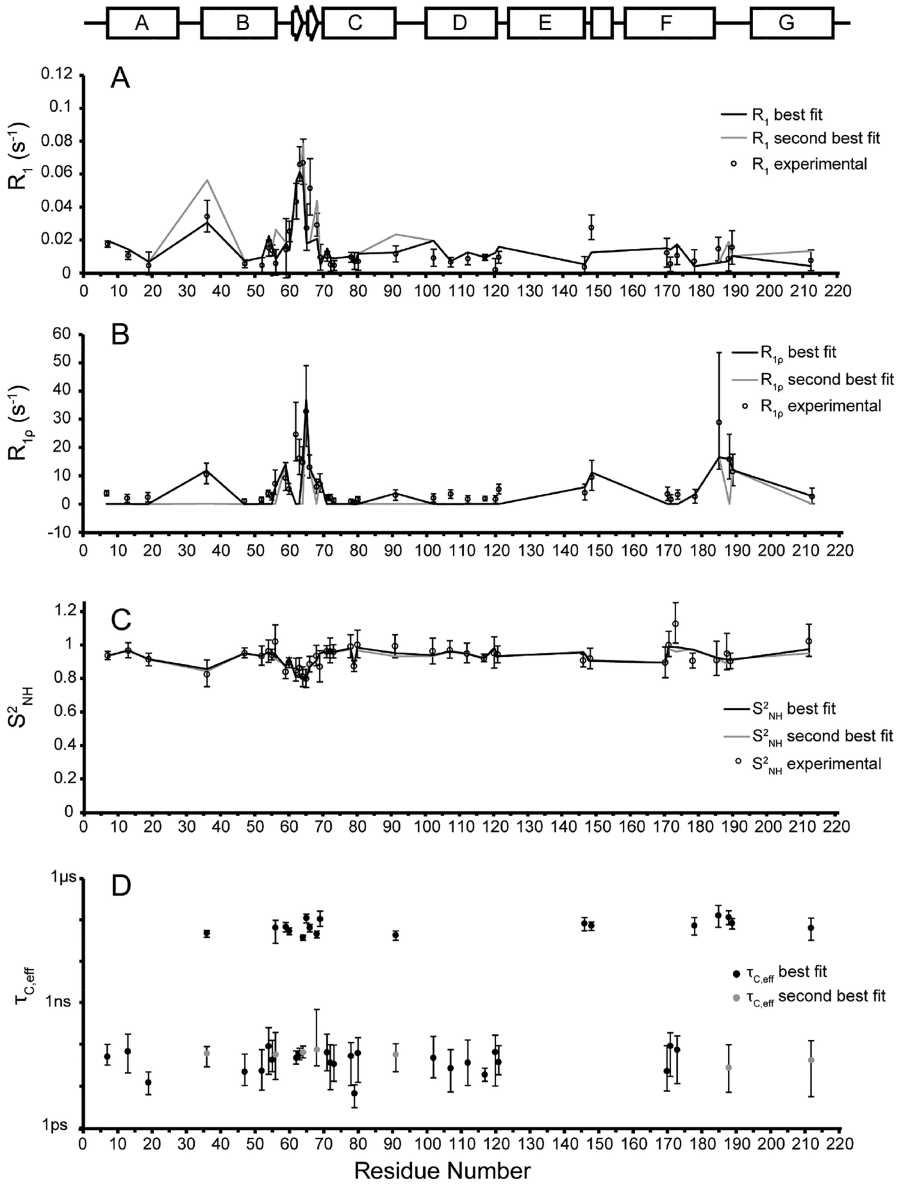

Figure 5. Simple Model Free fit results showing back calculated ^{15}N R_1, $R_{1\rho}$ and S^2_{NH} order parameter vs experimentally measured R_1 at 800 MHz (A), $R_{1\rho}$ at 800 MHz (B), and the S^2_{NH} order parameters (C). Best fit correlation times (D) are shown with uncertainties determined from Monte Carlo fitting analysis. For residues with two possible solutions on two distinct time scales, the best fit solution is shown as black circles, and the second best fit result is shown in gray. The second best fit solution is only shown if its population is greater than 10% of the total number of Monte Carlo fits performed.

the SMF fit returns the time scale which most significantly contributes to the experimental data.

The best fit time scales for the TM regions are in the 10 to 100 ps regime for all but seven intrahelical residues, E36, I56, A91, I146, N148, G178 and G212. Four of them (E36, A91, I146, N148) are located on the cytoplasmic sides of helices B, C, E. The best fit time scales for these residues are in the 10 to 100 ns regime, which is in agreement with the observed field- and temperature dependencies of the R_1 and $R_{1\rho}$ relaxation rates discussed above (Figures 3 and 4). I56 is on the extracellular edge of helix B near the structured BC loop region, and may be affected by the slower motion of that loop. Residues G178 and G212 are near the retinal binding pocket in the center of helices F and G, respectively. Their best fit time scales are in the 10 to 100 ns range, and may reflect the presence of complicated motional processes occurring on multiple time scales.

Relaxation rates and order parameters for most residues in the BC loop (I56−H69) are best fit with the 10 to 100 ns time scale motions, with the exception of residues E62 and A63 which are best fit by motions in the 10 to 100 ps regime (Tables S5−S6, Figure 5). The FG loop (I185−N194) is the only region where the SMF fit gives reasonable results with reduced χ^2 in the range of 0.3 to 2.8 (Table S6, Figure 5) with the dominant time scale in the 10 to 100 ns regime, which is consistent with the previously discussed R_1 and $R_{1\rho}$ field- and temperature dependent trends (Figures 3, 4; Figure S9 for I185 and G189 representative Monte Carlo histograms).

Modeling of Relaxation Rates Using a Local-Collective Extended Model Free Approach. High reduced χ^2 values and inconsistent time scales obtained using SMF fit for residues

DOI: 10.1021/jacs.7b03974
J. Am. Chem. Soc. 2017, 139, 9246−9258

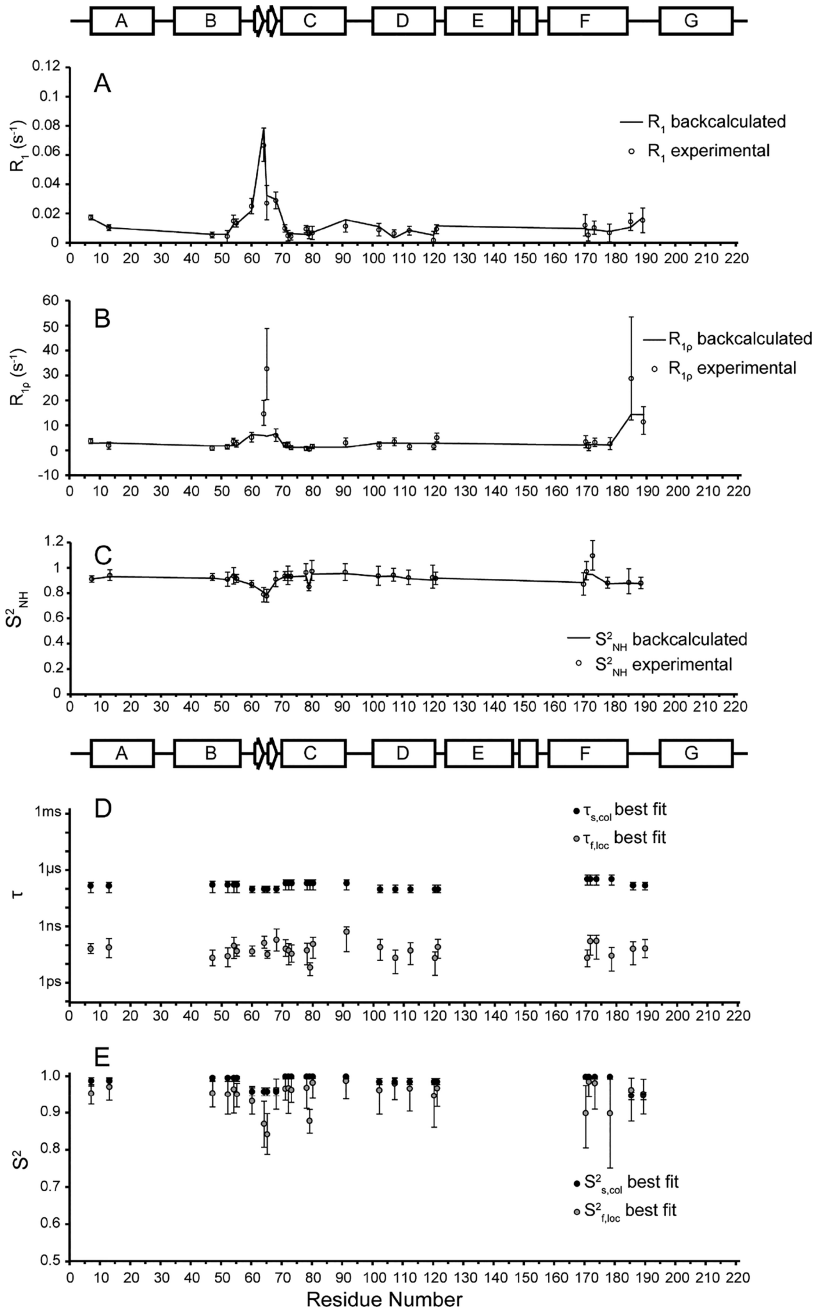

Figure 6. Local-collective Extended Model Free (EMF) fit results showing back calculated ^{15}N R_1, $R_{1\rho}$ and order parameter vs experimentally measured R_1 at 800 MHz (A), $R_{1\rho}$ at 800 MHz (B), and $^{15}N-^{1}H$ dipolar order parameters (C). Best fit local and collective motion correlation times (D) and order parameters (E) are shown with error bars determined from Monte Carlo fitting analysis (see Figure S13 for representative histograms).

located within the same structurally defined elements suggest that one needs to consider more than one motional degree of freedom in order to correctly interpret the experimental data. Consequently, we resorted to a version of Extended Model Free (EMF) approach,[77,78] in which the spectral density function $J(\omega)$ is modeled assuming the presence of fast and slow motions. In contrast to the typical implementation where both fast and slow motions are considered to be local,[39] we assume the fast component to be local and the slow component to correspond to collective motions extending over an entire secondary structure element:

$$J(\omega) = \frac{2}{5}(1 - S^2_{f,\mathrm{loc}})\frac{\tau_{f,\mathrm{loc}}}{1 + \omega^2\tau^2_{f,\mathrm{loc}}} + \frac{2}{5}S^2_{f,\mathrm{loc}}(1 - S^2_{s,\mathrm{col}})\frac{\tau_{s,\mathrm{col}}}{1 + \omega^2\tau^2_{s,\mathrm{col}}} \quad (9)$$

Each motion is characterized by its own order parameter and the time scale: $\tau_{s,\mathrm{col}}$ and $\tau_{f,\mathrm{loc}}$ correlation times describe slow and fast time scales, respectively, whereas $S^2_{s,\mathrm{col}}$ and $S^2_{f,\mathrm{loc}}$ are order parameters describing the amplitudes of slow and fast motions, respectively. The $S^2_{s,\mathrm{col}}$ and $S^2_{f,\mathrm{loc}}$ order parameters are related to the experimentally determined effective order parameter as $S^2_{\mathrm{NH}} = S^2_{s,\mathrm{col}}S^2_{f,\mathrm{loc}}$.

DOI: 10.1021/jacs.7b03974
J. Am. Chem. Soc. 2017, 139, 9246−9258

Among the considered secondary structure elements we include seven helices which are stabilized by intrahelical hydrogen bonds, as well as the BC and FG loops (Table S8). The BC loop is partially structured and contains an antiparallel beta-hairpin formed by two short beta strands involving residues V61-E62-A63 and Q66-I67-A68.[47,68] We expect that the slower time scale would correspond to a collective motion of this loop (discussed in the following). The FG loop, although not as well structurally defined as the BC loop, contains some beta structure acording to the CSI analysis, whereas the presence of a few nonexchangeble amides of G186, G189, G191, W192, I193 suggests strong stabilizing hydrogen bonds within the loop (Figure 3C).[47,68]

Elevated ^{15}N $R_{1\rho}$ rates for residues in the BC and FG loops provide a direct evidence for slow nanosecond to microsecond motions. Motions of other loops appear to also have a slow nanosecond component, as evident from the dependence of R_1 rates on the magnetic field strength (Figure 3), but they are less correlated between neighboring residues because of the lack of defined secondary structure. Thus, we do not apply the collective motion approximation to these loops, and exclude them from the EMF analysis.

Within each of the nine considered elements each residue was assigned the same slow time scale, order parameter and activation energy characterizing the common collective motion of the element, whereas the time scale, order parameter and activation energy characterizing the fast motions were kept residue-specific. The use of a common order parameter for a fragment implies that this fragment undergoes isotropic motion. In the case of a TM helix, this isotropic motion can be pictured as a combination of rotations about the helical axis and a random wobbling motion of the enitre helix. We note that because of the steric interhelical restraints anisotropic collecitve motions appear to be more likely. Such a possibility is explicitely taken into account in the 3D Gaussian Axian Fluctuation[46] simulation discussed below.

In our EMF fit we only consider data from residues for which all six experimentally measured parameters defined in Table 1 are available. We fit all parameters by minimizing reduced χ^2 defined in eq S6 using a proceedure detailed in the Supporting Information.

In general this model provides a better fit of the experimental data in the TM helical regions with an average reduced χ^2 ranging from 1.7 to 6.3 (Table S8). There is good agreement between the experimentally measured and back-calculated relaxation rates and dipolar order parameters for TM helices, as shown in Figures 6, S14, thus suggesting that the collective motion approximation is justified for the TM regions. Local fast motions occur on the 10−100 ps time scales for the majority of residues, have consistently lower corresponding order parameters (larger amplitudes) (Figure 6E, Tables S9−S10), and mostly higher activation energies (Tables S9−S10).

Whereas these motions make the dominant contributions to the back-calculated R_1 and S^2_{NH} values, the slower motional components (tens to hundreds of nanoseconds) of small amplitudes are required to adequately explain the relaxation and order parameter data for all seven helices ($S^2_{s,col}$ order parameters vary from 0.984 ± 0.007 for helix A to 0.995 ± 0.002 for helix C, Tables S9−S10). These order parameters correspond to small amplitudes of collective motions. However, we can not rule out a possibility of large structural rearragements between a highly populated state and a lowly populated state, as was shown by Zinkevich et al.[39]

While better reduced χ^2 of 4 is obtained for the BC loop, the collective slow motion approximation does not provide good quality fits for two residues A64 and G65 (Figure 6B), one of which, A64, represents the unstructured β-hairpin turn in the BC loop, suggesting that the rigid approximation is not entirely valid, and either additional motional degrees of freedom are present, or that the motion is anisotropic. Similarly, while an overall better fit is obtained for the FG loop (reduced χ^2 of 3.3, Table S8) the $R_{1\rho}$ relaxation rate for residue I185 is not reproduced by our model (Figure 6B).

Modeling of Relaxation Rates Using a Local-Collective Model Free-3D GAF Approach. As shown above, the modified EMF formalism with the slow motions modeled as isotropic collective motions of ordered domains, provides a better description of the data compared to the SMF formalism. In this last section, we consider whether an inclusion of anisotropy of slow motions is necessary to adequately model the data.[46,79]

To include the effects of anisotropy of the slow collective motions we make a simple change to the modified EMF. We keep the isotropic order parameter for the fast motions, $S^2_{f,loc}$, but replace the isotropic order parameter $S^2_{s,col}$ with a 3D Gaussian Axial Fluctuations variant $S^2_{s,\mu\nu}$, which parametrizes the slow collective motion as Gaussian fluctuations against three orthogonal axes α, β and γ:

$$S^2_{s,\mu\nu} = \frac{4\pi}{5} \sum_{l,k,k',m,m'}^{2} (-i)^{k-k'} e^{-\sigma_\alpha^2/l^2-\sigma_\beta^2(k^2+k'^2)/2-\sigma_\gamma^2(m^2+m'^2)/2} d^{(2)}_{kl}\left(\frac{\pi}{2}\right) d^{(2)}_{k'l}\left(\frac{\pi}{2}\right) d^{(2)}_{m'k'}\left(\frac{\pi}{2}\right) Y_{2m}(e_\mu) Y^*_{2m'}(e_\nu) \quad (10)$$

Here, Y_{2m} are the second spherical harmonics, $e_\mu = (\theta_\mu,\varphi_\mu)$ and $e_\nu = (\theta_\nu,\varphi_\nu)$ are the spherical coordinates of interactions μ and ν in the 3D GAF motion reference frame rigidly attached to molecular fragment (for autorelaxation $\mu = \nu$, and in our case these are the coordinates of the NH vector), $d^{(2)}_{kl}\left(\frac{\pi}{2}\right)$ are the reduced Wigner matrix elements, and σ_α, σ_β and σ_γ are amplitudes of fluctuations/rotations (expressed in radians) against the three respective axes of motion.

For the analysis we consider the same secondary structure fragments as in the local-collective EMF treatment. Since the orientation of the 3D GAF motion reference frame is not known a priori, we express the initial coordinates of NH vectors in the molecular frame and treat the two angles defining the orientation of the motional frame as fit parameters. Other than the modifications to the form of the spectral density the fitting procedure remains the same as for the local-collective EMF. We use the same data set as we did for the local-collective EMF, which gives enough data points to perform local-collective Model Free-3D GAF (MF-3D GAF) fit for helices B, C, D and F and for the BC loop.

As expected for a model containing more fit parameters the χ^2 is generally lower for the MF-3D GAF. In order to establish whether the improvement of the fit is statistically significant, we utilize Akaike's Information Criterion (AIC), which can be used for comparison of the non-nested models. In addition, since AIC is valid for infinite samples size, we also calculate Bayesian

DOI: 10.1021/jacs.7b03974
J. Am. Chem. Soc. 2017, 139, 9246−9258

Information Criterion (BIC) and AIC with correction for the finate sample sizes (AICc), which contain progressively larger penatly for the finate sample size (see Supporting Information, eqs S3−S5).

Overall, based on AIC, including anisotropy of slow motion results in statistically significant improvement of the fit for helices B and D, and for the BC loop. Based on BIC, which contains a larger penalty for the finate sample size, lower χ^2 from anisotropic model is statistically significant for helix D and for the BC loop. For helices C and F the improvement in fit is not statistically significant compared to the isotropic model of motion. On the basis of AICc the local-collective MF-3DGAF fit is not statistically significant for any of the secondary structure elements, which is not really surprising considering that AICc have the largest penalty for finate sample size and the number of available data points is rather low.

In order to fit other secondary elements we have also included previously published NCO dipolar order parameters[23] as restraints. With this additional data the AIC criterion suggests that the improvement from including anisotropy of slow motion is statistically significant for helix A, but not for the FG loop. The slow anisotropic motions obtained as a result of fitting the data to MF-3DGAF are summarized in Figure 7 for one of the monomers. Note that the motions are the same for all the monomers and the motional axes in different monomers are related by the C3 symmetry.

As expected, the amplitudes of the slow anisotropic motions are smaller compared to our previously published analysis[23] which explicitly neglected contribution from the fast motions. On the other hand, the directions of the anisotropic collective motions from the MF-3D GAF in the current analysis are similar to the ones from 3D GAF analysis in the previous study. The only exception is helix D where the overall motion is detected as a rotation around an axis approximately perpendicular to the long axis of helix. Since the amide vectors are approximately aligned with the long axis of helix, the direction of the axis of rotation can not be determined precisely without additional data such as, for example, ^{13}C relaxation rates.[15]

CONCLUSIONS

In summary, we used solid-state NMR relaxation and dipolar coupling measurements to characterize internal dynamics of a seven-helical membrane protein Anabaena Sensory Rhodopsin. We showed that at least two motional processes occurring on the picosecond and nanosecond time scales are required in order to correctly interpret the field- and temperature-dependent relaxation behavior. The relative contributions of these motional processes to the overall dynamics vary between the buried TM and solvent exposed regions of the receptor.

The inclusion of longitudinal relaxation rates into data analysis allowed estimating the fast local dynamics which contribute significantly to nuclear spin relaxation within TM helices (local order parameters $S^2_{f,\mathrm{loc}}$ range between 0.89 and 0.99). The refined time scales and order parameters for the slower nanosecond collective motions appear to be slower and more restrticted than what had been estimated by us earlier[23] (refined collective motion order parameter $S^2_{s,\mathrm{col}}$ is greater than 0.98 on a time scale of hundreds of nanoseconds). Such limited collective dynamics can be attributed to the tightly packed and highly constrained (2D crystalline) transmembrane environment.

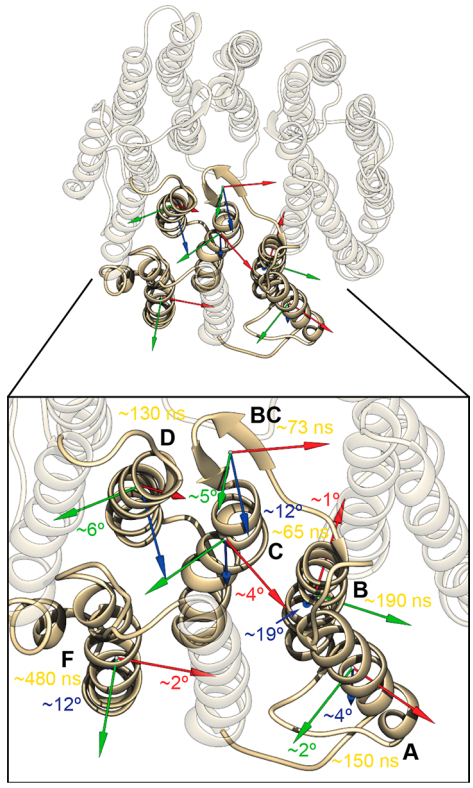

Figure 7. Amplitudes and time scales of anisotropic slow collective motions obtained from local-collective Model Free-3D GAF (MF-3DGAF) analysis of ^{15}N R_1, $R_{1\rho}$ and NH order parameters, as well as NCO order parameters published previously.[23] Approximate rotations against different axes are indicated in a font of the same color. Time scales are indicated in yellow. Motions are illustrated for only one of the three monomers with the motions in the other monomers being related by C3 symmetry. The origins of the frames of reference for the motions are arbitrary.

In contrast, nanosecond motions (~100 ns) of two extracellular BC and FG loops are much less restricted ($S^2_{s,\mathrm{col}}$ of ~0.95 and 0.94, respectively), with their amplitudes approaching the amplitudes of fast local motions ($S^2_{f,\mathrm{loc}}$ ranging between 0.84 and 0.97, ~10 ps time scale). The collective motions contribute significantly to the $R_{1\rho}$ rates and accordingly, the time scales of the slower motional components are in agreement with our previous estimates.[23]

The inclusion of anisotropy of motion for the collective motions of ordered elements leads to statistically significant improvement of fit for helices A, B, C, D and the BC loop. The extracted directions of motions are generally consistent with the general directions of motions for secondary structure elements obtained from the Normal Mode Analysis of ASR trimer (Figure S15). Interestingly, the collective motion of the BC loop modulates the size of the extracellular opening for the "channel" in the center of the ASR trimer, and in this context, is reminiscent of a motion of a camera shutter. We note, however, that the role of the opening in the center of the ASR trimer is not known, nor does it play functional role in a structurally similar trimer formed by bacteriorhodopsin.

Although there was no sufficient $R_{1\rho}$ data to draw quantitative conclusions about the dynamics of the cytoplasmic side of ASR, qualitative analysis of the temperature dependence of the longitudinal R_1 rates indicate that the amplitudes of slower nanosecond motions increase toward the cytoplasmic

DOI: 10.1021/jacs.7b03974
J. Am. Chem. Soc. 2017, 139, 9246−9258

ends of helices and in cytoplasmic loops. ASR interacts with its soluble transducer (ASRT) in the dark.[45,80] In the process of its function, ASR undergoes a series of conformational changes, including between the ASRT-bound and unbound states.[80] The cytoplasmic interface of ASR is likely involved in the interaction with the soluble cytoplasmic transducer. An increased plasticity of the cytoplasmic sides of helices and loops may play role in the mechanism of structural transition between ASRT-bound and unbound states.

Among microbial rhodopsins, bacteriorhodopsin (BR) is one of the best-characterized homologues of ASR. Neutron diffraction studies of site-specifically deuterated BR demonstrated that the extracellular sides of BR helices are more rigid than the rest of the protein,[81] whereas MD simulations specifically showed that the distributions of atomic coordinates on the extracellular side are more localized than those on the cytoplasmic side.[82] This apparent plasticity of the cytoplasmic face of BR was proposed to facilitate photoexcited transition to the M_o intermediate state, which has more open conformation on the intracellular side. An increased plasticity of the cytoplasmic side of ASR may play similar role and be related to the transition to the active M-intermediate state responsible for the release of the cytoplasmic transducer upon photoactivation.

■ ASSOCIATED CONTENT

Supporting Information

The Supporting Information is available free of charge on the ACS Publications website at DOI: 10.1021/jacs.7b03974.

Experimental pulse sequences, data analysis and fitting procedures, additional figures, tables of experimentally determined order parameters, R_1, $R_{1\rho}$ relaxation rates, and extracted motional amplitudes, correlation times, and activation energies (PDF)

Movie S1 (MPG)

■ AUTHOR INFORMATION

Corresponding Author

*vladizha@uoguelph.ca

ORCID

Vladimir Ladizhansky: 0000-0003-1314-4014

Notes

The authors declare no competing financial interest.

■ ACKNOWLEDGMENTS

We thank Professor Leonid S. Brown of the University of Guelph for many useful discussions. This research was supported by the Natural Sciences and Engineering Research Council of Canada (Discovery Grant RGPIN-2014-04547 to V.L.), the Canada Foundation for Innovation, and the Ontario Ministry of Research and Innovation. D.G. is a recipient of an NSERC Postgraduate Doctoral Scholarship. C.P. held NSERC USRA award. J.R.L. acknowledges funding from European Research Council under the European Union's Seventh Framework Programme (FP/2007-2013)/ERC Grant Agreement 639907, BBSRC Grant BB/L022761/1 and Gates Foundation OPP1160394.

■ REFERENCES

(1) Henzler-Wildman, K.; Kern, D. *Nature* **2007**, *450*, 964−972.
(2) Richards, F. M. *Carlsberg Res. Commun.* **1979**, *44*, 47−63.
(3) Kovermann, M.; Rogne, P.; Wolf-Watz, M. *Q. Rev. Biophys.* **2016**, *49*, e6.
(4) Lisi, G. P.; Loria, J. P. *Chem. Rev.* **2016**, *116*, 6323−6369.
(5) Palmer, A. G.; Massi, F. *Chem. Rev.* **2006**, *106*, 1700−1719.
(6) Palmer, A. G. *Chem. Rev.* **2004**, *104*, 3623−3640.
(7) Kossiakoff, A. A. *Nature* **1982**, *296*, 713.
(8) Woodward, C.; Simon, I.; Tuchsen, E. *Mol. Cell. Biochem.* **1982**, *48*, 135−160.
(9) Frauenfelder, H.; Sligar, S. G.; Wolynes, P. G. *Science* **1991**, *254*, 1598−1603.
(10) Hvidt, A.; Nielsen, S. O. *Adv. Protein Chem.* **1966**, *21*, 287−386.
(11) Mittermaier, A.; Kay, L. E. *Science* **2006**, *312*, 224−228.
(12) Jarymowycz, V.; Stone, M. J. *Chem. Rev.* **2006**, *106*, 1624−1671.
(13) Schanda, P.; Ernst, M. *Prog. Nucl. Magn. Reson. Spectrosc.* **2016**, *96*, 1−46.
(14) Lamley, J. M.; Lewandowski, J. R. In *eMagRes.*; John Wiley & Sons, Ltd: Chichester, UK, 2016; pp 1423−1434.
(15) Lewandowski, J. R. *Acc. Chem. Res.* **2013**, *46*, 2018−2027.
(16) Krushelnitsky, A.; Reichert, D.; Saalwächter, K. *Acc. Chem. Res.* **2013**, *46*, 2028−2036.
(17) Lamley, J. M.; Öster, C.; Stevens, R. A.; Lewandowski, J. R. *Angew. Chem., Int. Ed.* **2015**, *54*, 15374−15378.
(18) Lu, M.; Hou, G.; Zhang, H.; Suiter, C. L.; Ahn, J.; Byeon, I.-J. L.; Perilla, J. R.; Langmead, C. J.; Hung, I.; Gor'kov, P. L.; Gan, Z.; Brey, W.; Aiken, C.; Zhang, P.; Schulten, K.; Gronenborn, A. M.; Polenova, T. *Proc. Natl. Acad. Sci. U. S. A.* **2015**, *112*, 14617−14622.
(19) Smith, A. A.; Testori, E.; Cadalbert, R.; Meier, B. H.; Ernst, M. *J. Biomol. NMR* **2016**, *65*, 171−191.
(20) Lewandowski, J. R.; Halse, M. E.; Blackledge, M.; Emsley, L. *Science* **2015**, *348*, 578−581.
(21) Vugmeyster, L.; Clark, M. A.; Falconer, I. B.; Ostrovsky, D.; Gantz, D.; Qiang, W.; Hoatson, G. L. *J. Biol. Chem.* **2016**, *291*, 18484−18495.
(22) Hoop, C. L.; Lin, H.-K.; Kar, K.; Magyarfalvi, G.; Lamley, J. M.; Boatz, J. C.; Mandal, A.; Lewandowski, J. R.; Wetzel, R.; van der Wel, P. C. A. *Proc. Natl. Acad. Sci. U. S. A.* **2016**, *113*, 201521933.
(23) Good, D. B.; Wang, S.; Ward, M. E.; Struppe, J.; Brown, L. S.; Lewandowski, J. R.; Ladizhansky, V. *J. Am. Chem. Soc.* **2014**, *136*, 2833−2842.
(24) Wang, S.; Ladizhansky, V. *Prog. Nucl. Magn. Reson. Spectrosc.* **2014**, *82*, 1−26.
(25) Murray, D. T.; Das, N.; Cross, T. A. *Acc. Chem. Res.* **2013**, *46*, 2172−2181.
(26) Radoicic, J.; Lu, G. J.; Opella, S. J. *Q. Rev. Biophys.* **2014**, *47*, 249−283.
(27) Wylie, B. J.; Do, H. Q.; Borcik, C. G.; Hardy, E. P. *Mol. Phys.* **2016**, *114*, 3598−3609.
(28) Schmidt, P.; Thomas, L.; Müller, P.; Scheidt, H. A.; Huster, D. *Chem. - Eur. J.* **2014**, *20*, 4986−4992.
(29) Barré, P.; Yamaguchi, S.; Saitô, H.; Huster, D. *Eur. Biophys. J.* **2003**, *32*, 578−584.
(30) Struts, A. V.; Salgado, G. F. J.; Brown, M. F. *Proc. Natl. Acad. Sci. U. S. A.* **2011**, *108*, 8263−8268.
(31) Struts, A. V.; Salgado, G. F. J.; Martínez-Mayorga, K.; Brown, M. F. *Nat. Struct. Mol. Biol.* **2011**, *18*, 392−394.
(32) Ye, L.; Van Eps, N.; Zimmer, M.; Ernst, O. P.; Scott Prosser, R. *Nature* **2016**, *533*, 265−268.
(33) Saurel, O.; Iordanov, I.; Nars, G.; Demange, P.; Le Marchand, T.; Andreas, L. B.; Pintacuda, G.; Milon, A. *J. Am. Chem. Soc.* **2017**, *139*, 1590−1597.
(34) Lamley, J. M.; Lougher, M. J.; Sass, J.; Rogowski, M. *Phys. Chem. Chem. Phys.* **2015**, *17*, 21997−22008.
(35) Lewandowski, J. R.; Sass, H. J.; Grzesiek, S.; Blackledge, M.; Emsley, L. *J. Am. Chem. Soc.* **2011**, *133*, 16762−16765.
(36) Krushelnitsky, A.; DeAzevedo, E.; Linser, R.; Reif, B.; Saalwächter, K.; Reichert, D. *J. Am. Chem. Soc.* **2009**, *131*, 12097−12099.
(37) Li, W.; McDermott, A. E. *J. Biomol. NMR* **2009**, *45*, 227−232.

DOI: 10.1021/jacs.7b03974
J. Am. Chem. Soc. 2017, 139, 9246−9258

(38) Krushelnitsky, A.; Zinkevich, T.; Reichert, D.; Chevelkov, V.; Reif, B. *J. Am. Chem. Soc.* **2010**, *132*, 11850−11853.
(39) Zinkevich, T.; Chevelkov, V.; Reif, B.; Saalwächter, K.; Krushelnitsky, A. *J. Biomol. NMR* **2013**, *57*, 219−235.
(40) De Paëpe, G.; Giraud, N.; Lesage, A.; Hodgkinson, P.; Böckmann, A.; Emsley, L. *J. Am. Chem. Soc.* **2003**, *125*, 13938−13939.
(41) Krushelnitsky, A.; Bräuniger, T.; Reichert, D. *J. Magn. Reson.* **2006**, *182*, 339−342.
(42) Giraud, N.; Blackledge, M.; Böckmann, A.; Emsley, L. *J. Magn. Reson.* **2007**, *184*, 51−61.
(43) Lewandowski, J. R.; Sein, J.; Sass, H. J.; Grzesiek, S.; Blackledge, M.; Emsley, L. *J. Am. Chem. Soc.* **2010**, *132*, 8252−8254.
(44) Asami, S.; Porter, J. R.; Lange, O. F.; Reif, B. *J. Am. Chem. Soc.* **2015**, *137*, 1094−1100.
(45) Jung, K.-H.; Trivedi, V. D.; Spudich, J. L. *Mol. Microbiol.* **2003**, *47*, 1513−1522.
(46) Lienin, S. F.; Bremi, T.; Brutscher, B.; Brüschweiler, R.; Ernst, R. R. *J. Am. Chem. Soc.* **1998**, *120*, 9870−9879.
(47) Shi, L.; Kawamura, I.; Jung, K.-H.; Brown, L. S.; Ladizhansky, V. *Angew. Chem.* **2011**, *123*, 1338−1341.
(48) Shi, L.; Ladizhansky, V. *Methods Mol. Biol.* **2012**, *895*, 153−165.
(49) Ammann, C.; Meier, P.; Merbach, A. *J. Magn. Reson.* **1982**, *46*, 319−321.
(50) Thurber, K. R.; Tycko, R. *J. Magn. Reson.* **2009**, *196*, 84−87.
(51) Pines, A.; Gibby, M. G.; Waugh, J. S. *J. Chem. Phys.* **1973**, *59*, 569.
(52) Hartmann, S. R.; Hahn, E. L. *Phys. Rev.* **1962**, *128*, 2042−2053.
(53) Baldus, M.; Petkova, A. T.; Herzfeld, J.; Griffin, R. G. *Mol. Phys.* **1998**, *95*, 1197−1207.
(54) Takegoshi, K.; Nakamura, S.; Terao, T. *Chem. Phys. Lett.* **2001**, *344*, 631−637.
(55) Morcombe, C. R.; Gaponenko, V.; Byrd, R. A.; Zilm, K. W. *J. Am. Chem. Soc.* **2004**, *126*, 7196−7197.
(56) Fung, B. M.; Khitrin, A. K.; Ermolaev, K. *J. Magn. Reson.* **2000**, *142*, 97−101.
(57) Hohwy, M.; Jaroniec, C. P.; Reif, B.; Rienstra, C. M.; Griffin, R. G. *J. Am. Chem. Soc.* **2000**, *122*, 3218−3219.
(58) Bennett, A. E.; Rienstra, C. M.; Auger, M.; Lakshmi, K. V.; Griffin, R. G. *J. Chem. Phys.* **1995**, *103*, 6951.
(59) Banigan, J. R.; Traaseth, N. J. *J. Phys. Chem. B* **2012**, *116*, 7138−7144.
(60) Kotecha, M.; Wickramasinghe, N. P.; Ishii, Y. *Magn. Reson. Chem.* **2007**, *45*, S221−S230.
(61) Verel, R.; Ernst, M.; Meier, B. H. *J. Magn. Reson.* **2001**, *150*, 81−99.
(62) Westfeld, T.; Verel, R.; Ernst, M.; Böckmann, A.; Meier, B. H. *J. Biomol. NMR* **2012**, *53*, 103−112.
(63) Delaglio, F.; Grzesiek, S.; Vuister, G. W.; Zhu, G.; Pfeifer, J.; Bax, A. D. *J. Biomol. NMR* **1995**, *6*, 277−293.
(64) Keller, R. *The Computer Aided Resonance Assignment Tutorial*, 1st ed.; Verlag, C., Ed.; Goldau, Switzerland, 2004.
(65) Rienstra, C. M.; Hohwy, M.; Mueller, L. J.; Jaroniec, C. P.; Reif, B.; Griffin, R. G. *J. Am. Chem. Soc.* **2002**, *124*, 11908−11922.
(66) Allen, F. H.; Kennard, O.; Watson, D. G.; Brammer, L.; Orpen, A. G.; Taylor, R. *J. Chem. Soc., Perkin Trans. 2* **1987**, No. No.12, S1.
(67) Wang, S.; Munro, R. A.; Kim, S. Y.; Jung, K.; Brown, L. S.; Ladizhansky, V. *J. Am. Chem. Soc.* **2012**, *134*, 16995−16998.
(68) Wang, S.; Munro, R.; Shi, L.; Kawamura, I.; Okitsu, T.; Wada, A.; Kim, S.-Y.; Jung, K.-H.; Brown, L. S.; Ladizhansky, V. *Nat. Methods* **2013**, *10*, 1007−1012.
(69) Ward, M. E.; Wang, S.; Munro, R.; Ritz, E.; Hung, I.; Gor, P. L.; Jiang, Y.; Liang, H.; Brown, L. S.; Ladizhansky, V. *Biophys. J.* **2015**, *108*, 1683−1696.
(70) Wang, S.; Shi, L.; Okitsu, T.; Wada, A.; Brown, L. S.; Ladizhansky, V. *Biomol. NMR Assignments* **2013**, *7*, 19−22.
(71) Kurbanov, R.; Zinkevich, T.; Krushelnitsky, A. *J. Chem. Phys.* **2011**, *135*, 184104.
(72) Wylie, B. J.; Sperling, L. J.; Frericks, H. L.; Shah, G. J.; Franks, W. T.; Rienstra, C. M. *J. Am. Chem. Soc.* **2007**, *129*, 5318−5319.
(73) Wylie, B. J.; Franks, W. T.; Rienstra, C. M. *J. Phys. Chem. B* **2006**, *110*, 10926−10936.
(74) Lipari, G.; Szabo, A. *J. Am. Chem. Soc.* **1982**, *104*, 4559−4570.
(75) Lipari, G.; Szabo, A. *J. Am. Chem. Soc.* **1982**, *104*, 4546−4559.
(76) Ward, M. E.; Wang, S.; Krishnamurthy, S.; Hutchins, H.; Fey, M.; Brown, L. S.; Ladizhansky, V. *J. Biomol. NMR* **2014**, *58*, 37−47.
(77) Clore, G. M.; Szabo, A.; Bax, A.; Kay, L. E.; Driscoll, P. C.; Gronenborn, A. M. *J. Am. Chem. Soc.* **1990**, *112*, 4989−4991.
(78) Chevelkov, V.; Fink, U.; Reif, B. *J. Am. Chem. Soc.* **2009**, *131*, 14018−14022.
(79) Lewandowski, J. R.; Sein, J.; Blackledge, M.; Emsley, L. *J. Am. Chem. Soc.* **2010**, *132*, 1246−1248.
(80) Kondoh, M.; Inoue, K.; Sasaki, J.; Spudich, J. L.; Terazima, M. *J. Am. Chem. Soc.* **2011**, *133*, 13406−13412.
(81) Wood, K.; Grudinin, S.; Kessler, B.; Weik, M.; Johnson, M.; Kneller, G. R.; Oesterhelt, D.; Zaccai, G. *J. Mol. Biol.* **2008**, *380*, 581−591.
(82) Jang, H.; Crozier, P. S.; Stevens, M. J.; Woolf, T. B. *Biophys. J.* **2004**, *87*, 129−145.

DOI: 10.1021/jacs.7b03974
J. Am. Chem. Soc. 2017, 139, 9246−9258